Microstructure, mechanical properties, Electrical resistivity, and corrosion behavior of $(AlCr)_x(HfMoNbZr)_{1-x}$ films

Jianjun Kang[a], Hao Liu[a], Hao Du[a,b*], Jie Shi[a], Linlin Wang[c], Liuquan Yang[d], Houfu Dai[e,f*]

[a] *School of Mechanical Engineering, Guizhou University, Guiyang 550025, PR China*

[b] *State Key Laboratory of Public Big Data, Guizhou University, Guiyang 550025, PR China*

[c] *College of Engineering, Mathematics and Physical Sciences, University of Exeter, Exeter EX4 4QF, United Kingdom*

[d] *School of Mechanical Engineering, University of Leeds, Leeds LS2 9JT, United Kingdom*

[e] *Department of Mechanical Engineering, Shantou University, Shantou 515063, PR China*

[f] *State Key Laboratory of Advanced Design and Manufacturing for Vehicle Body, Hunan University, Changsha 410082, PR China*

* Corresponding authors: Hao Du, Houfu Dai

E-mail address: hdu3@gzu.edu.cn, houfudai@hnu.edu.cn

Postal address: School of Mechanical Engineering, Guizhou University, Guiyang, 550025, PR China

Abstract

Refractory high-entropy alloys (RHEAs) have emerged as a new class of materials due to their exceptional properties such as high strength, high-temperature stability, and potential for corrosion resistance. In this study, we investigate the effect of Al and Cr co-alloying on the crystal structure, mechanical properties, electrical resistivity, and corrosion resistance of HfMoNbZr film. $(AlCr)_x(HfMoNbZr)_{1-x}$ films were grown using direct current magnetron sputtering, with $Al_{50}Cr_{50}$ and $Hf_{25}Mo_{25}Nb_{25}Zr_{25}$ target co-sputtering. Our findings reveal that all films possess a B2-type BCC fine-grained crystallite structure. Moreover, an increase in AlCr content results in an increase in hardness and electrical resistivity, which can be attributed to the stronger directionally angular bonds and higher local lattice distortion caused by Al atoms, as confirmed by density functional theory (DFT) calculations. Additionally, the $(AlCr)_x(HfMoNbZr)_{1-x}$ films exhibit excellent corrosion resistance in 3.5 wt% NaCl solution, as indicated by a corrosion current below 10^{-8} A/cm^2. Remarkably, at P_{AlCr} = 90 W, the current density reaches a minimum value of $4.85 \pm 0.43\times10^{-9}$ A/cm^2. These results demonstrate the tunable properties of RHEAs through element alloying, which offers promising opportunities for various applications.

Keywords: High entropy alloy film, magnetron sputtering, Hardness, Corrosion behavior, density functional theory calculation

1 Introduction

The proposal of high entropy alloys (HEAs) in 2004[1] sparked a wave of innovative scientific research. HEAs broke the conventional one or two major elements alloying design strategy with the constituent metallic elements are approximately 5 to 13 and are mixed in equimolar or near equimolar ratios in the range of 5 ~ 35 at.%[1,2]. Four core effects, including the high entropy effect, lattice distortion effect, sluggish diffusion effect, and the 'cocktail' effect, were shown to confer superior properties on HEAs[1–4]. These special effects provide HEA with advantages over conventional alloys, such as high corrosion resistance[5] , good mechanical properties[6], and thermal stability[7].

Refractory HEAs consisting of transition metals in groups 4 to 6 which with high melting points (e.g., Cr, Hf, Mo, Nb, Ta, Ti, V, W, Zr, etc.) have exhibited excellent mechanical properties and thermal stability, and can be extended to thin film synthesis[8–10] . For instance, WTaNbMo and WTaNbMoV alloys with single disordered BCC solid solution phases have higher strengths than conventional superalloys (Inconel 718 and Haynes 230) at temperatures above 1000°C[11]. Additionally, the NbMoTaW thin film shows a nanocrystalline solid-solution phase with BCC structure, accompanied by a hardness of 12 GPa and an electrical resistivity of 168 μΩ·cm, which makes it useful as a protective coating and as an electrical resistors in nanofabricated devices[12]. Apart from that, the refractory metal elements are considered "dissolution inhibitors" because they possess high cohesion energy and oxide generation energy, which are indicators of metal dissolution difficulty and passivation ability, respectively[13]. $Ti_{1.5}ZrTa_{0.5}Nb_{0.5}Hf_{0.5}$ refractory HEA films, for example, exhibits excellent corrosion resistance with a corrosion current density of about 10^{-8} A/cm^2 when exposed to phosphate buffer saline (BPS) solution at 37 ± 1 °C[14].

The unique composition of HEAs allows the properties of the alloys to be adjusted by changing the composition or by adding additional elements. Al acts as a BCC phase stabilizer in 3*d* transition metal (TM) and improves the mechanical properties of HEAs[15].

Investigations of VNbMoTaWAl HEA refractory films show that Al alloying effectively reduces the grain size and improves the film density, thereby improving the film hardness[16]. The same improvement in hardness is observed in $(NbTiVZr)_{100-x}Al_x$ HEA films[17]. Additionally, Cr has excellent passivation properties, and its role in HEA corrosion resistance has also been confirmed in studies [18,19]. Although both Al and Cr can be classified as "passivation promoters" according to the criteria of cohesion energy and oxide generation energy[13], the influence of Al on the corrosion resistance of HEAs remains controversial. For instance, the $Al_x(CoCrFeNi)_{100-x}$ HEA films[20] exhibit excellent corrosion resistance in 3.5 wt.% NaCl solution, but the corrosion resistance gradually decreased with increasing Al content. Therefore, exploring the evolution of hardness and corrosive behavior of AlCr co-doped refractory-based HEA films is of great interest.

In this study, a series of innovative refractory films with the composition of $(AlCr)_x(HfMoNbZr)_{1-x}$ are synthesized using direct current magnetron sputtering technique, where various AlCr contents are incorporated. The influence of AlCr content on the phase structure, mechanical properties, electrical resistivity, and corrosion resistance (in 3.5 wt. % NaCl solution) of HfMoNbZr HEA films is investigated. Additionally, to comprehend the alteration in film crystallographic structure and mechanical properties, the phase structure and electronic structure, such as the electronic density of states (DOS), partial density of states (PDOS), and electron localization function (ELF), are calculated for $(AlCr)_{59}(HfMoNbZr)_{41}$ film.

2 Experimental details

The $(AlCr)_x(HfMoNbZr)_{1-x}$ films were deposited onto one-side polished 0.5 mm-thick Si (100) wafer through direct current magnetron sputtering (dcMS) in a high vacuum chamber with a base pressure of 2×10^{-3} Pa. The process utilized 3-inch $Hf_{25}Mo_{25}Nb_{25}Zr_{25}$ (99.95% purity) and $Al_{50}Cr_{50}$ (99.80% purity) targets, which were placed at a distance of 11 cm from the substrate holder. Before the deposition, all substrates underwent sequential cleaning with petroleum

ether and ethanol in an ultrasonic bath for 10 minutes each, and were then dried using air before installation onto the substrate holder. During the deposition process, the work pressure was maintained at 0.45 Pa by fixing the flow rate of Ar (99.997% purity) at 40 sccm. The targets were sputter cleaned for approximately 5 minutes to eliminate contaminants, during which the substrate shutter was closed. The target power of $Hf_{25}Mo_{25}Nb_{25}Zr_{25}$ (P_{MC}) was set to 200 W and the $Al_{50}Cr_{50}$ target power (P_{AlCr}) was set to 0 W, 50 W, 70 W, 90 W, 110 W, and 130 W, respectively, for film depositions. All depositions were conducted at room temperature (without external heating) and floating substrate bias. The substrates were fixed on a substrate holder with a rotation speed of 30 rpm, and the deposition time for all series was set to 120 minutes.

The cross-sectional morphologies of $(AlCr)_x(HfMoNbZr)_{1-x}$ films were investigated using a scanning electron microscope (SEM, Sigma 300, Zeiss) with an acceleration voltage of 3.0 kV. Elemental compositions were determined using the energy-dispersive X-ray spectrometry (EDS, Smartedx, Zeiss) equipped in the same instrument. X-ray diffraction (XRD) was operated in a high-resolution XRD diffractometer (XRD, Smart Lab, Rigaku) in Bragg-Brentano (θ-2θ) geometry with Cu Kα radiation (λ = 1.540597 Å). The recorded 2θ range was 30 – 80° with a step size of 0.01° at a scan speed of 2°/min. The accelerating voltage and emission current was set to 30 kV and 40 mA, respectively. X-ray photoelectron spectroscopy (XPS) was carried out for films grown at P_{AlCr} = 0 W and 90 W (both before and after corrosion) using XPS instrument (Thermo Fisher Scientific K-Alpha). A monochromator aluminum source (Al Kα radiation at 1486.7 eV, 6 mA) accompanied by a light spot diameter of 400 μm was utilized. For the XPS survey spectra, the electron energy analyzer was operated at a pass energy of 150 eV and step size of 1 eV. To obtain high-resolution spectra, the pass energy and step size were set to 50 eV and 0.1 eV, respectively. The spectra for both the raw surface and the sputter-etched surface were acquired. An Ar^+ ion beam was used to etch the surface with depths of 10, 20, and 30 nm, respectively. For each spectrum, the binding energy scale was calibrated by examining the raw valence band spectrum, where the Fermi edge was set as "0

eV" to avoid problems caused by the use of C 1s peaks (see Fig. S1 for the etching depth of 30 nm case) [21,22]. The interval time between the experiments, i.e., film deposition and corrosion test, and the XPS measurements were kept identical for films grown at P_{AlCr} = 0 W and 90 W.

The hardness (H) and elastic modulus (E) of the $(AlCr)_x(HfMoNbZr)_{1-x}$ films were determined using nanoindentation measurements (TTX-NHT3, Anton Paar) with a Berkovich diamond indenter tip in the Oliver-Pharr analysis model[23]. To ensure a penetration depth less than 10% of the film thickness, the load was set to 10 mN. For each sample, 5 indentations were performed, and H and E values were calculated by averaging the results. The electrical resistivity of the $(AlCr)_x(HfMoNbZr)_{1-x}$ films was implemented via a precision resistivity tester (HPS2662, HELPASS), using a four-point probe method. The sheet resistance obtained by the probe was used to calculate the electrical resistivity along with the film thickness evaluated by SEM. The electrical resistivity of each sample was obtained by averaging six measurements. To evaluate the corrosive behavior of the $(AlCr)_x(HfMoNbZr)_{1-x}$ films, the electrochemical experiments were performed using the electrochemical workstation (DH7000, DONGHUA) in a conventional three-electrode cell. A commercial saturated calomel electrode (SCE) and a 20×20 mm^2 Pt plate was used as the reference electrode and the auxiliary electrode, respectively. The test area for the working electrode, i.e., $(AlCr)_x(HfMoNbZr)_{1-x}$ film, was 1 cm^2. Prior to the potentiodynamic polarization test, all specimens were exposed in the 3.5 wt.% NaCl solution for 1800 s to reach a relatively stable value of the open circuit potential (OCP). The potentiodynamic polarization measurements were performed in an applied potential range from −500 mV to +1500 mV versus the OCP at a sweep rate of 1 mV/s. Electrochemical parameters such as corrosion potential (E_{corr}), corrosion current density (I_{corr}), Tafel anode slope (β_a), and Tafel cathode slope (β_c) were obtained by extrapolating the linear portion of polarization curves. To ensure reproducibility and accuracy, the measurements were performed at least three times.

The Special Quasi-random Structure (SQS) model of $(AlCr)_{59}(HfMoNbZr)_{41}$ film deposited at P_{AlCr} in 90 W is generated using mcsqs module of Alloy-Theoretic Automated

Toolkit (ATAT) code[24]. The BCC structure has 100 atoms, of which the conventional cell is amplified into 5×5×2 supercell. The density functional theory (DFT) calculations were performed via the Vienna ab initio calculation simulation package (VASP)[25]. The projector augmented-wave (PAW)[26] method was employed to simulate the interaction between ion-electron. The general gradient approximation (GGA) given by Perdew-Burke-Ernzerhof (PBE) was selected as exchange-correlation function in DFT calculations[27]. The plane wave cut-off energy was set to 400 eV, and the k-mesh over the Brillouin zone was 4 × 4 × 4 Monkhorst-Pack sampling. The energy was converged to less than 1 meV/atom in this study. The equilibrium volume was obtained by fitting the third-order Birch-Murnaghan equation of state (EOS)[28]. The post-processing and charge density analysis was virtualized via VASPKIT [28]. A two-step relaxation calculation was performed for the ionic relaxation calculation.

3 Results

3.1 Composition and crystal structure

Elemental composition of $(AlCr)_x(HfMoNbZr)_{1-x}$ film as a function of the P_{AlCr} is shown in Fig. 1. The concentrations of Al and Cr increase as P_{AlCr} increases, and reaches the maximum percentage of 31.5 at. % and 35.5 at. %, respectively, at a P_{AlCr} of 130 W. The contents of Hf, Mo, Nb, and Zr elements are nearly, with a slightly higher content of Hf compared to its percentage in the multicomponent target. It should be noted that even at a relatively low P_{AlCr} of 50 W, which is at the edge of discharge ignition, the elemental concentrations of Al and Cr are higher than those sputtered out from the multicomponent target. This is mainly due to the higher sputter yield of Al and Cr compared to other elements and their higher percentage in the AlCr target.

Fig. 2 illustrates the cross-sectional SEM morphologies of the as-deposited $(AlCr)_x(HfMoNbZr)_{1-x}$ films. The film thickness is significantly increased as P_{AlCr} ranges from 0 to 130 W, and all films show a typical glass-like feature consistent with studies elsewhere[29] No obvious voids or cracks is observed.

Fig. 3 (a) shows x-ray diffractograms of as-deposited $(AlCr)_x(HfMoNbZr)_{1-x}$ films and the $(AlCr)_{0.59}(HfMoNbZr)_{0.41}$ (calculated) crystal. A B2-type body-centered cubic (BCC) crystallite structure with reflections at $2\theta = 36.76° \sim 39.11°$ are seen for all the as-deposited films, where a (110) plane is identified. The broadened peak obtained by the films shows crystallite size refinement analogous to the descriptions in Ref. [30] and Ref. [31]. The position of the 110 peak gradually shifts towards higher diffraction angles with the increase of P_{AlCr}. Compared with the $P_{AlCr} = 0$ W case, the diffraction peak intensity for AlCr alloyed HfMoNbZr films is weakened, while the peak intensities are not further decreased as P_{AlCr} increases. The overall peaks for as-deposited films are, however, positioned at lower angles as compared with the theoretical positions calculated using DFT method. We speculate that this phenomenon could result from the increased lattice distortion under the ion irradiation of rare gas ions. To gain more insight into the change in the film crystallographic structure, the out-of-plane lattice constant and the FWHM of the as-deposited films are calculated and shown in Fig. 3 (b) and Fig. 3 (c), respectively. both the out-of-plane lattice constant and the FWHM gradually decrease with the increase of P_{AlCr}. Also, it is noticed that the FWHM has an opposing trend at P_{AlCr} of 110 W. To assess the reliability of the computational constants set, the theoretical lattice constant was also calculated for $(AlCr)_{0.59}(HfMoNbZr)_{0.41}$ (calculated) crystal (see Fig.3 (b)). The calculated lattice constant (3.17 Å) is lower, with a difference of 4.7% (<5%), than that of as-deposited films at P_{AlCr} = 90 W (3.326 Å), which is in line with the peak position variation shown in Fig. 3 (a).

3.2 Mechanical properties

The hardness (H) and the elastic modulus (E) of $(AlCr)_x(HfMoNbZr)_{1-x}$ films are depicted in Fig. 4 (a). As is seen in Fig. 4(a), H and E of HfMoNbZr alloy film is 8.95 ± 0.29 GPa and 144.02 ± 2.10 GPa, respectively. With the increase of P_{AlCr}, H of films shows an upward trend, and the largest value of 11.67 ± 0.53 GPa is obtained as P_{AlCr} = 130 W. We also observe a decrease of E as P_{AlC} increases from 110 W to 130 W. H/E and H^3/E^{*2} correlate with the elastic recovery behavior of film and the resistance of film against plastic deformation, respectively

[32]. Herein, H/E and H^3/E^{*2} values are estimated and shown in Fig. 4(b). It is seen that H/E and H^3/E^{*2} values are enhanced following the increase of P_{AlCr}.

3.3 Electrical resistivity

Fig. 5 shows the electrical resistivity of the $(AlCr)_x(HfMoNbZr)_{1-x}$ films as a function of P_{AlCr}. The electrical resistivity increases monotonously from the minimum value of 153.66 μΩ.cm to the maximum value of 207.95 μΩ.cm as P_{AlCr} increases. Additionally, the resistivity of $(AlCr)_x(HfMoNbZr)_{1-x}$ films, ranging from 153.66 μΩ.cm to 207.95 μΩ.cm, fall within the range of other multi-component (high-entropy) alloy films [33].

3.4 Corrosion properties

Fig. 6 depicts the potentiodynamic polarization curves of $(AlCr)_x(HfMoNbZr)_{1-x}$ films in 3.5 wt.% NaCl solution. The potentiodynamic polarization curves of the $(AlCr)_x(HfMoNbZr)_{1-x}$ films all possessed similar compositions. At around 500 mV, the films' polarization curves displayed a turning point, where they demonstrated an inclination towards rapid potential increase and stable current. The turning point is an obvious passivating phenomenon. The locally magnified view (shown in Fig. 6) illustrated that the passivation zone of the films, after the addition of AlCr, does not follow a vertical straight line; instead, it presents an "S" like curve, which is a typical secondary passivation phenomenon. Additionally, when the potential reached approximately 1150mV, the films' polarization curves exhibited similar small current spikes with a "serration shape", known as "metastable pitting"[34,35], indicating impending pitting of the film. However, as shown from the partial magnification in Fig. 6, and Table1, the films grown at P_{AlCr} of 50 W and 70 W did not show pitting in the tested range, followed by the decrease of the pitting potential (E_{pit}) of each film with the increasing P_{AlCr} as $P_{AlCr} \geq 90$ W. To quantitatively assess the films' corrosion resistance properties, various corrosion resistance parameters, such as E_{corr}, I_{corr}, β_a, β_c, and the polarization resistance (R_p), were evaluated using Tafel parameters. The polarization resistance (R_p) was calculated using the Stern-Geary equation [36]:

$$R_{\mathrm{p}} = \frac{\beta_{\mathrm{a}} \times \beta_{\mathrm{c}}}{2.303 \times I_{\mathrm{corr}} \times (\beta_{\mathrm{a}} + \beta_{\mathrm{c}})} \quad (1)$$

The initial passivation current density (I_{pass}) value represents the current density of the passivation region, and it is determined at 600 mV (the middle of the initial passivation region of the potentiodynamic polarization curve)[37].

Table 1 provides all the electrochemical parameters. With an increase in P_{AlCr}, both I_{corr} and E_{corr} gradually decrease. The $(\mathrm{AlCr})_x(\mathrm{HfMoNbZr})_{1-x}$ film grown at P_{AlCr} = 90 W exhibits the lowest I_{corr} (4.85 nA/cm^2), which is significantly lower (an order of magnitude) as compared with that of P_{AlCr} = 0 W case (11 nA/cm^2). Furthermore, R_{p} increases with the increasing P_{AlCr} and reaches a maximum value of 2595.12 kΩ·cm^2 at 90W. While the I_{pass} of all film samples remains at a low order of magnitude (3.5 ~ 3.8 μA/cm^2), the I_{pass} shows an increasing trend with an increase in P_{AlCr}.

To have a further understanding of the film corrosion mechanism, XPS is conducted to characterize the chemical state of the films' surfaces before and after corrosion, as well as the valence state associated with the depth of the oxide film following the gradual removal of the outermost film surface by Ar^+ sputter-etching. High-resolution spectra of the films at depths of 0, 10, 20, and 30 nm are presented in Fig. 7. Figs. 7(a-e) show high-resolution spectra corresponding to the elements for the P_{AlCr} = 0 W film in its before- and after-corrosion states. The results clearly indicate that the raw film surface in the before-corrosion state is mainly composed of HfO_2, ZrO_2, Nb_2O_5, with a relatively small proportion of MoO_2 oxides [38]. In contrast, the intensity of the peaks corresponding to all elemental oxides becomes stronger for the films after the corrosion test. With the sputter-etching depth of 10 nm, the corresponding oxide peaks in the Mo 3d and Nb 3d spectra of the film in the after-corrosion state disappear (see Fig. 7(b) and (c)). However, faint oxide peaks in the Hf 4f (Fig. 7(a)) and Zr 3d (Fig. 7(d)) spectra are still present even with the sputter-etching depth of up to 30 nm for the film after the corrosion test, implying that the passivation layer of the film is mainly composed of HfO_2 and ZrO_2. Notably, the O 1s spectrum is separated into two parts, i.e., O^{2-} species (~530.34 eV) and

the OH^- species (~532.19 eV) [38], corresponding to the formation of metal oxides, hydroxides, and adsorbed hydrates, respectively, as suggested in Ref. [39]. The intensity of the hydroxide peak becomes stronger after the corrosion test and is significantly reduced after 10 nm-depth sputter-etching. The high-resolution spectra of the $P_{AlCr} = 90$ W (Figs. 7(f-l)) show that peaks for oxides or hydroxides in Mo 3d (Fig. 7(g)), Nb 3d (Fig. 7(h)), and Cr 2p (Fig. 7(k)) spectra disappear at the sputter-etching depth $\geqslant$ 10 nm when the film is in both before- and after-corrosion states. In contrast, peaks for oxides in the Hf 4f (Fig. 7(f)) and Zr 3d (Fig. 7(i)) spectra disappear at the sputter-etching depth of 20 nm for the as-deposited film, while faint oxide peaks still exist at the same depth for the after-corrosion film. In the Al 2p spectrum (Fig. 7(j)), the peak for oxide still exists at the sputter-etching depth of 30 nm for both before- and after-corrosion films, implying that the majority of Al_2O_3 is present in the film as compared with other metallic oxides or hydroxides. In regards to the O 1s spectrum (see Fig.7(l)), a comparable phenomenon is observed in the O 1s spectrum of the $P_{AlCr} = 90$ W film as compared to that of the $P_{AlCr} = 0$ W film. Specifically, the peak intensity corresponding to OH^- species becomes more pronounced after corrosion, and as observed from the sputter-etched film, OH^- species are only present in the layer with a depth of less than 10 nm. It is noteworthy that Mo is oxidized to higher valence oxides (MoO_3) for both $P_{AlCr} = 0$ W and $P_{AlCr} = 90$ W cases, which is different from other metallic elements (see Fig. S4) [40].

It should also be noted that the singlet peak (~224 eV) observed in the Mo 3d spectrum is associated with the photoelectron peak of Hf $4d_{3/2}$ [41]. Additionally, the peak detected at the binding energy value of ~213 eV in the Nb 3d spectrum corresponds to the Hf $4d_{5/2}$ photoelectron peak, which overlaps in the Nb region. Similar phenomena occur in the XPS spectra of other elements in all measured films and therefore will not be discussed further [41,42].

3.5 Electronic structure and chemical bonding

Fig. 8 illustrates the total density of states (TDOS) and partial density of states (PDOS) of $(AlCr)_{0.59}(HfMoNbZr)_{0.41}$ (calculated) crystal. The energy range of the crystal, mainly consisting of the distribution range of bonding electron energy range from -9.28 to 0 eV, and the conduction band region above the Fermi energy level (0 to 2.09 eV). DOS around the E_F is related to the corrosion resistant performance of the alloy [43,44]. As seen in Fig. 8 (a), the majority of the contribution to the TDOS comes from the Cr atom, whereas Al, with a content similar to Cr, contributes less near the E_F. The other constituent elements, including Hf, Mo, Nb, and Zr, show a similar contribution to the TDOS. As is shown in Fig. 8 (b), the contributions of Hf, Mo, Nb, Zr, and Cr are mainly from the *d* states which are different from that of Al, where *s* and *p* states both make contributions. In the energy range from -4.38 to -9.28 eV of the PDOS of Al atom (Fig. 8 (b)), the hybridization of *s*-*p*-*d* orbitals increases the small sharp peaks below -5 eV, which composited from *s* states of Al, and *p* and *d* states from transition metal elements.

To virtualize the interatomic interactions in crystals, the electron localization function (ELF) is carried out and shown in Fig. 9. As seen in Fig. 9, the ELF values > 0.8, strong directional bonds, mainly positioned at the vicinity of Al atoms. In contrast, Hf, Mo, Nb, Zr, and Cr atoms are surrounded by low value ELF (~0.3) indicating delocalized valence electrons. More important, the low ELF value (~0.1) of Cr atom proves the high level contribution to TDOS, which is consistent with the observations in Fig. 8. In general, in the present metallic bonded alloy, the valence electrons of the transition-metal atoms tend to delocalize while Al atom is more likely under localized state.

4 Discussion

4.1 Evolution of crystallographic structure

The results obtained from cross-sectional morphologies (Fig. 2) and θ-2θ x-ray diffractograms (Fig. 3) demonstrate that the as-deposited $(AlCr)_x(HfMoNbZr)_{1-x}$ films possess a B2-type BCC

fine-grained crystallite structure, which is consistent with the findings in Ref.[29]. The formation of BCC structure is highly dependent on the constituent elements as Mo, Nb, and Cr tends to form BCC crystal structure at low temperature, and Al and Zr are esteemed as stabilizers of such structure[15,16,45]. Especially, electronic interaction between Al and refractory metals (RMs) results in the occupation of *d* shell of RMs and the *sp–d* orbital hybridization of Al, which leads to the formation of the BCC structure[15]. This phenomenon is in accordance with the calculations in Section 3.5. Another factor of Al-induced BCC stabilization lays on the negative enthalpy of Al when mixed with the other constituent elements (refer to Table S1) [15,46, 47], where valence electron concentration (VEC) plays a decisive role in determining the solid solution phases in HEAs, i.e., a lower VEC (<6.87) favors the steady exist of BCC-type solid solutions (see Table S2). The lattice constant decreases with the increasing P_{AlCr} (see Fig. 3) can be explained by the interaction of Al with refractory metals (RMs), where the high electron density and high Fermi level of Al promote electron transfer with RMs. This strong electronic interaction between Al and RMs leads to a shortened bond between Al-RM which even shorter than the sum of the corresponding metallic radii. Moreover, the incorporation of Cr, which has a smaller atomic radius (refer to Table S1), also contributes to the decrease in lattice constant. It is important to note that the HfMoNbZr film is a medium-entropy alloy film (ΔS_{mix} < 1.5 R = 12.471 J/K·mol) which should compare with the high-entropy alloy $(AlCr)_x(HfMoNbZr)_{1-x}$ film (see Table S2).

4.2 Mechanical property

An increase in P_{AlCr} is seen to correspondingly increase the hardness of the $(AlCr)_x(HfMoNbZr)_{1-x}$ film, as depicted in Fig. 4. This strengthening mechanism is attributed to the introduction of Al and Cr, which leads to an increased δ (as seen in Table S2) and local lattice distortion of Al atoms (as seen in Fig. 9). Herein, we estimate the local lattice distortion (Δd) for Al, Cr, Hf, Mo, Nb, and Zr in the BCC-structured $(AlCr)_{0.59}(HfMoNbZr)_{0.41}$ lattice by the following equation:

$$\Delta d = \frac{1}{N}\sum_{i}\sqrt{(x_i - x_i')^2 + (y_i - y_i')^2 + (z_i - z_i')^2} \quad (2)$$

Where $(x_i,\ y_i,\ z_i)$ and $(x_i',\ y_i',\ z_i')$ are the reduced coordinates of the unrelaxed and relaxed positions of atom *i*, respectively. The resulting Δd for Al, Cr, Hf, Mo, Nb, and Zr is 0.705, 0.108, 0.120, 0.015, 0.159, and 0.013, respectively. In this regard, Al atoms contributes more to the lattice distortion as compared with the other constituent atoms, and the higher content of Al in the lattice, thereby, increase the degree of lattice distortion. As the lattice distortion degree within the film increases with the increasing P_{AlCr}, the motion of dislocations are more likely impeded and as a result film hardness are enhanced. In addition, it is suggested that the strengthened interatomic bonds between Al and RMs lead to a densified atomic packing lattice[16]. This have been conformed in Fig. 9, where electrons localized in the vicinity of the Al atom are in high ELF values. Similarly, the stronger directionally angular bonds around Al are proved to result in significant improvement of hardness of bulk alloys[48].

4.3 Electrical resistivity

According to Matthiessen's rule, the total resistivity of a material can be broken down into four components, which are represented by the equation[49]:

$$\rho = \rho_b + \rho_{im} + \rho_s + \rho_g \quad (3)$$

Here, ρ_{b} denotes bulk or geometry-independent resistivity determined by electron scattering from phonons, ρ_{im} and ρ_{g} are the resistivity caused by scattering at impurities and grain boundaries, and ρ_{s} is the resistivity from electron-surface scattering.

It is generally accepted that the grain size of a material is inversely proportional to the concentration of grain boundaries. However, in the case of $(\mathrm{AlCr})_{\mathrm{x}}(\mathrm{HfMoNbZr})_{1\text{-}\mathrm{x}}$ films, the crystallite size actually increases with increasing P_{AlCr}, as shown in Fig. 3. This would typically be expected to decrease the electrical resistivity of the film, as resistivity is mainly influenced by scattering at grain boundaries[50]. However, in this case, the electrical resistivity of the film actually increases with the increase in P_{AlCr}, contradicting this expectation. The increase in

electrical resistivity (up to ~70%) can be attributed to lattice distortion, as lattice strain in films effectively retards the movement of electrons, reducing the electron mean free path by inducing electron scattering[51,52]. As depicted in Fig. 3(b), all the as-deposited films have severe lattice distortion as compared with the calculated unstained lattice. Furthermore, it was identified in Section 4.3 that the local lattice distortion of Al atoms is more significant than that of other constituent atoms. This may explain the increased electrical resistivity of the film when subjected to higher P_{AlCr}. We also speculate that the increased resistivity of $(AlCr)_x(HfMoNbZr)_{1-x}$ with the increase P_{AlCr} is partly due to the formation of directional bonds by Al (see Fig. 9), i.e., the increasing Al content bring more directional bonds and thus retards the movement of electrons. Additionally, XPS measurements (Fig. 7) reveal a comparatively high accumulation of oxygen on the surface, forming a native oxide layer on the as-deposited films. The higher Al and Cr content will thereby decrease the dielectric constant of this layer and thus decrease the conductivity[53,54].

4.4 Electrochemical corrosion characteristics

Considerable differences arise in the passivation zone of $(AlCr)_x(HfMoNbZr)_{1-x}$ films due to changes in the elemental concentration of Al and Cr. The change in the elemental concentration of Al and Cr generates considerable differences in the passivation zone of the $(AlCr)_x(HfMoNbZr)_{1-x}$ films. The initial I_{pass} increases with the increase of P_{AlCr}, revealing low stability of the oxide layer formed on the AlCr-rich films as compared with that of non-AlCr-added film, as I_{pass} reveals the anodic dissolution rate for passive metals [55]. The "metastable pitting", when the potential reaches around 1150 mV, is attributed to the continuous breaking and formation of the passive film. Uhlig et al. [56] proposed that both O^{2-} and Cl^- anions can be adsorbed onto metal surfaces. When O^{2-} is adsorbed, the metal passivates whereas the adsorption of chloride does not produce a passive surface. Thus, above a critical potential, where Cl^- adsorption is favored over O^{2-} adsorption, a breakdown of passivity occurs. Another possible explanation of this phenomenon (After the AlCr doping, the I_{corr} decreases and I_{pass} increases) is related to the higher resistivity of native oxide layer mainly composed of Al-O

and Cr-O as compared with RM-O, i.e., higher amount of Al-O and Cr-O in the native oxide layer will increase the over-all film resistivity as discussed in the previous section.

As shown in Fig. 7 and Fig. S4, Mo oxide does not form in the native oxide layer of $(AlCr)_x(HfMoNbZr)_{1-x}$ films, which differs from HfMoNbZr films. This indicates that the high chemical activity of Al and Cr preferentially forms a protective layer on the film surface to prevent the oxidation of other elements. The breakdown of this layer is the basis of the collapse of the primary passivation layer, leading to localized pitting and the transport of ions, which contributes to the formation of a secondary passivation layer. The corresponding reaction process is given as[57]:

$$Cr_2O_3 + 5H_2O \rightarrow 2Cr_2O_4^{2-} + 10H^+ + 6e^- \quad (4)$$

As the corrosion continues, the passive film becomes thinner. Owing to the continued growth and diffusion of pitting, adjacent pits merge and the film is exposed to the solution. When the Cl^- concentration in the pit is not enough to induce the formation of a stable pit, re-passivation occurs [58]. The "metastable pitting" observed in the secondary passivation zone when the scanning potential rises is attributed to further oxidation Mo oxides and continued passivation of other elements to passivate the damaged passive film, as demonstrated by the presence Mo^{6+} in the XPS results (see Fig. 7), and the decrease of the relative content of metallic state elements.

The unstable passivation zone observed in the $(AlCr)_x(HfMoNbZr)_{1-x}$ film could be due to the following reasons: As Al tends to form a thick and porous passivation layer on the surface, the increased Al oxide content on the film surface with the increasing P_{AlCr} will facilitate the breakdown of the passive film under the action of aggressive Cl^- [59,20]. In addition, the O 1s spectrum in Fig. 7 and Fig. S4. shows that the addition of Al and Cr increases the relative OH^- content in the film, where the hydroxide in the passive film exhibits lower density than the oxide. The increase of OH^- ratio will as a result decreases the protective function of the passive film [59,20].

Aluminum is a highly active metal and tends to form oxides, which is consistent with the fact that the corrosion potential of the film samples shows a decreasing trend with the increase of P_{AlCr}. It is well known that the corrosion potential is a thermodynamic parameter that indicates the tendency of a sample to corrode, the lower the corrosion potential the higher the tendency of the sample to corrode. According to previous studies[20,59] , Cr_2O_3 in the passive films plays a key role in protection. Simultaneously, depending on the experimental results, this work also confirms the role of Cr in improving the corrosion resistance of $(AlCr)_x(HfMoNbZr)_{1-x}$ films. Based on the I_{corr} to measure the material's uniform corrosion sensitivity, it can be used as a criterion to determine the anodic dissolution rate of different materials[55]. thus, I_{corr} seems more vital. The $(AlCr)_x(HfMoNbZr)_{1-x}$ film with P_{AlCr} = 90 W exhibits the best corrosion resistance with the lowest I_{corr} of 4.85 nA/cm^2, the highest R_p of 2595.12 KΩ·cm^2, and the highest 1359 mV of E_{pit}. A certain degree of AlCr doping increases the corrosion resistance of the film. The $(AlCr)_x(HfMoNbZr)_{1-x}$ film in this work has the I_{corr} on the order of nA (see Table1), indicating that the film has excellent corrosion resistance.

Based on the above analysis, the superior corrosion resistance of the film can be explained. $(AlCr)_x(HfMoNbZr)_{1-x}$ films were composed of a single BCC solid-solution phase with a homogeneous microstructure, absence of defects that increase corrosion susceptibility. For the nanocrystalline films prepared by magnetron sputtering, "layer to layer" nanocrystalline structures with high grain boundaries, make the grain boundary path becomes circuitous and tortuous and provided continuous protection to corrosive ions[29]. This is different from columnar or large-size crystal structures that provide preferential channels for corrosive agents[60]. On the other hand, the $(AlCr)_x(HfMoNbZr)_{1-x}$ films consist of corrosion-resistant elements (Cr, Hf, Mo, Nb, and Zr) which possess a strong capacity of passivation and are easy to form oxide films with dense packing structure which make the Cl^- hard to penetrate[34,4]. In addition, as the Fig. 8 shown, except for Al, the PDOS of all transition metal elements have a pseudo-energy gap at the Fermi energy level and are not zero, which means that the bonding

ability of transition metal elements is strong and their metal oxide formed with oxygen has strong covalent bonds to resist corrosion [44].

5 Conclusion

The study investigated the microstructure, mechanical properties, electrical resistivity, and corrosion resistance of $(AlCr)_x(HfMoNbZr)_{1-x}$ films with varying AlCr contents, which were deposited on Si (001) using DC magnetron sputtering. The films were found to have a BCC structure, which is consistent with first-principles calculations, with a (110) preferential orientation. Results showed that both hardness and resistivity increased with higher AlCr content, ranging from 8.95 to 11.67 GPa and 153.66 to 207.95 μΩ.cm, respectively. In addition, AlCr alloying effectively reduced the I_{corr} of the films in 3.5 wt.% NaCl solution. The smallest I_{corr} value of 4.85 nA/cm^2 was achieved at P_{AlCr} = 90 W, with the highest R_p of 2595.12 kΩ·cm^2 and the initial I_{pass} maintained at μA/cm^2 order of magnitude. The findings demonstrate that the corrosion resistance and mechanical properties of $(AlCr)_x(HfMoNbZr)_{1-x}$ films can be significantly improved by Al and Cr co-alloying, which can serve as a reference for future research on the properties of AlCr co-doped refractory-based HEA films.

Acknowledgments

The work was supported financially by the financial support from the National Natural Science Foundation of China (Grant No. 52165021, 51805102, 52105178, and 12162008) and the Natural Science Foundation of Guizhou Province (Grant No. [2020]1Y228). Dr. Jianjun Hu at University of South Carolina is appreciated for the help and support for DFT calculations. H. Du is grateful for the backing of the State Key Laboratory of Public Big Data, Guizhou University.

CRediT authorship contribution statement

Jianjun kang: Conceptualization, Investigation, Data curation, Formal analysis, Writing – original draft. **Hao Liu:** Conceptualization, Investigation, Data curation, Writing – review & editing. **Hao Du:** Project administration, Conceptualization, Supervision, Writing – review &

editing, Funding acquisition. **Jie Shi:** Investigation, Data curation, Formal analysis, Writing – review & editing. **Linlin Wang**: Conceptualization, Investigation, Data curation, Writing – review & editing. **Liuquan Yang**: Conceptualization, Investigation, Writing – review & editing. **Houfu Dai:** Project administration, Conceptualization, Writing – review & editing, Funding acquisition.

Data availability

The data that support these findings are available from the corresponding author on request.

Competing interests

The authors declare no competing interests.

Appendix A. Supplementary data

Supplementary data to this article can be found online at

References

[1] J.-W. Yeh, S.-K. Chen, S.-J. Lin, J.-Y. Gan, T.-S. Chin, T.-T. Shun, C.-H. Tsau, S.-Y. Chang, Nanostructured High-Entropy Alloys with Multiple Principal Elements: Novel Alloy Design Concepts and Outcomes, Adv. Eng. Mater. 6 (2004) 299–303. https://doi.org/10.1002/adem.200300567.

[2] M. Zhang, X. Zhou, X. Yu, J. Li, Synthesis and characterization of refractory TiZrNbWMo high-entropy alloy coating by laser cladding, Surf. Coat. Technol. 311 (2017) 321–329. https://doi.org/10.1016/j.surfcoat.2017.01.012.

[3] X. Sun, X. Cheng, H. Cai, S. Ma, Z. Xu, T. Ali, Microstructure, mechanical and physical properties of FeCoNiAlMnW high-entropy films deposited by magnetron sputtering, Appl. Surf. Sci. 507 (2020) 145131. https://doi.org/10.1016/j.apsusc.2019.145131.

[4] H. Du, R. Shu, R. Boyd, A. le Febvrier, U. Helmersson, P. Eklund, D. Lundin, Evolution of microstructure and properties of TiNbCrAlHfN films grown by unipolar and bipolar high-power impulse magnetron co-sputtering: The role of growth temperature and ion bombardment, Surf. Coat. Technol. (2023) 129389. https://doi.org/10.1016/j.surfcoat.2023.129389.

[5] S. Zheng, Z. Cai, J. Pu, C. Zeng, S. Chen, R. Chen, L. Wang, A feasible method for the fabrication of VAlTiCrSi amorphous high entropy alloy film with outstanding anti-corrosion property, Appl. Surf. Sci. 483 (2019) 870–874. https://doi.org/10.1016/j.apsusc.2019.03.338.

[6] D. Dou, X.C. Li, Z.Y. Zheng, J.C. Li, Coatings of FeAlCoCuNiV high entropy alloy, Surf. Eng. 32 (2016) 766–770. https://doi.org/10.1080/02670844.2016.1148380.

[7] S.-B. Hung, C.-J. Wang, Y.-Y. Chen, J.-W. Lee, C.-L. Li, Thermal and corrosion properties of V-Nb-Mo-Ta-W and V-Nb-Mo-Ta-W-Cr-B high entropy alloy coatings, Surf. Coat. Technol. 375 (2019) 802–809. https://doi.org/10.1016/j.surfcoat.2019.07.079.

[8] R. Shu, H. Du, G. Sadowski, M.M. Dorri, J. Rosen, M.A. Sortica, D. Primetzhofer, D. Lundin, A. le Febvrier, P. Eklund, Multicomponent TixNbCrAl nitride films deposited by dc and high-power impulse magnetron sputtering, Surf. Coat. Technol. 426 (2021) 127743. https://doi.org/10.1016/j.surfcoat.2021.127743.

[9] C. Cheng, X. Zhang, M.J.R. Haché, Y. Zou, Magnetron co-sputtering synthesis and nanoindentation studies of nanocrystalline (TiZrHf)x(NbTa)1−x high-entropy alloy thin films, Nano Res. 15 (2022) 4873–4879. https://doi.org/10.1007/s12274-021-3805-1.

[10] H. Cheng, Z. Pan, Y. Fu, X. Wang, Y. Wei, H. Luo, X. Li, Review—Corrosion-Resistant High-Entropy Alloy Coatings: A Review, J Electrochem Soc. 168 (2021) 111502. https://doi.org/10.1149/1945-7111/ac34d0.

[11] O.N. Senkov, G.B. Wilks, J.M. Scott, D.B. Miracle, Mechanical properties of Nb25Mo25Ta25W25 and V20Nb20Mo20Ta20W20 refractory high entropy alloys, Intermetallics. 19 (2011) 698–706. https://doi.org/10.1016/j.intermet.2011.01.004.

[12] H. Kim, S. Nam, A. Roh, M. Son, M.-H. Ham, J.-H. Kim, H. Choi, Mechanical and electrical properties of NbMoTaW refractory high-entropy alloy thin films, Int. J. Refract. Met. Hard Mater. 80 (2019) 286–291. https://doi.org/10.1016/j.ijrmhm.2019.02.005.

[13] C.D. Taylor, P. Lu, J. Saal, G.S. Frankel, J.R. Scully, Integrated computational materials engineering of corrosion resistant alloys, Npj Mater Degrad. 2 (2018) 6. https://doi.org/10.1038/s41529-018-0027-4.

[14] N.S. Peighambardoust, A.A. Alamdari, U. Unal, A. Motallebzadeh, In vitro biocompatibility evaluation of Ti1.5ZrTa0.5Nb0.5Hf0.5 refractory high-entropy alloy film for orthopedic implants: Microstructural, mechanical properties and corrosion behavior, J. Alloys Compd. 883 (2021) 160786. https://doi.org/10.1016/j.jallcom.2021.160786.

[15] Z. Tang, M.C. Gao, H. Diao, T. Yang, J. Liu, T. Zuo, Y. Zhang, Z. Lu, Y. Cheng, Y. Zhang, K.A. Dahmen, P.K. Liaw, T. Egami, Aluminum Alloying Effects on Lattice Types, Microstructures, and Mechanical Behavior of High-Entropy Alloys Systems, JOM. 65 (2013) 1848–1858. https://doi.org/10.1007/s11837-013-0776-z.

[16] S.K. Bachani, C.-J. Wang, B.-S. Lou, L.-C. Chang, J.-W. Lee, Microstructural characterization, mechanical property and corrosion behavior of VNbMoTaWAl refractory high entropy alloy coatings: Effect of Al content, Surf. Coat. Technol. 403 (2020) 126351. https://doi.org/10.1016/j.surfcoat.2020.126351.

[17] L.-C. Chang, Y.-C. Lu, C.-H. Hsueh, Effects of aluminum addition on microstructures and mechanical properties of NbTiVZr high-entropy alloy nitride films, Intermetallics. 156 (2023) 107868. https://doi.org/10.1016/j.intermet.2023.107868.

[18] A.Y. Gerard, J. Han, S.J. McDonnell, K. Ogle, E.J. Kautz, D.K. Schreiber, P. Lu, J.E. Saal, G.S. Frankel, J.R. Scully, Aqueous passivation of multi-principal element alloy Ni38Fe20Cr22Mn10Co10: Unexpected high Cr enrichment within the passive film, Acta Mater. 198 (2020) 121–133. https://doi.org/10.1016/j.actamat.2020.07.024.

[19] D.H. Xiao, P.F. Zhou, W.Q. Wu, H.Y. Diao, M.C. Gao, M. Song, P.K. Liaw, Microstructure, mechanical and corrosion behaviors of AlCoCuFeNi-(Cr,Ti) high entropy alloys, Mater. Des. 116 (2017) 438–447. https://doi.org/10.1016/j.matdes.2016.12.036.

[20] Y. Shi, B. Yang, P.D. Rack, S. Guo, P.K. Liaw, Y. Zhao, High-throughput synthesis and corrosion behavior of sputter-deposited nanocrystalline Alx(CoCrFeNi)100-x combinatorial high-entropy alloys, Mater. Des. 195 (2020) 109018. https://doi.org/10.1016/j.matdes.2020.109018.

[21] G. Greczynski, L. Hultman, Reliable determination of chemical state in x-ray photoelectron spectroscopy based on sample-work-function referencing to adventitious carbon: Resolving the myth of apparent constant binding energy of the C 1s peak, Appl. Surf. Sci. 451 (2018) 99–103. https://doi.org/10.1016/j.apsusc.2018.04.226.

[22] G. Greczynski, L. Hultman, X-ray photoelectron spectroscopy: Towards reliable binding energy referencing, Prog. Mater. Sci. 107 (2020) 100591. https://doi.org/10.1016/j.pmatsci.2019.100591.

[23] W.C. Oliver, G.M. Pharr, An improved technique for determining hardness and elastic modulus using load and displacement sensing indentation experiments, J. Mater. Res. 7 (1992) 1564–1583. https://doi.org/10.1557/JMR.1992.1564.

[24] A. van de Walle, Multicomponent multisublattice alloys, nonconfigurational entropy and other additions to the Alloy Theoretic Automated Toolkit, Calphad. 33 (2009) 266–278. https://doi.org/10.1016/j.calphad.2008.12.005.

[25] G. Kresse, J. Furthmüller, Efficiency of ab-initio total energy calculations for metals and semiconductors using a plane-wave basis set, Comput. Mater. Sci. 6 (1996) 15–50. https://doi.org/10.1016/0927-0256(96)00008-0.

[26] P.E. Blöchl, Projector augmented-wave method, Phys. Rev. B. 50 (1994) 17953–17979. https://doi.org/10.1103/PhysRevB.50.17953.

[27] G. Kresse, D. Joubert, From ultrasoft pseudopotentials to the projector augmented-wave method, Phys. Rev. B. 59 (1999) 1758–1775. https://doi.org/10.1103/PhysRevB.59.1758.

[28] V. Wang, N. Xu, J.-C. Liu, G. Tang, W.-T. Geng, VASPKIT: A user-friendly interface facilitating high-throughput computing and analysis using VASP code, Comput. Phys. Commun. 267 (2021) 108033. https://doi.org/10.1016/j.cpc.2021.108033.

[29] S. Zhao, L. He, X. Fan, C. Liu, J. Long, L. Wang, H. Chang, J. Wang, W. Zhang, Microstructure and chloride corrosion property of nanocrystalline AlTiCrNiTa high entropy alloy coating on X80 pipeline steel, Surf. Coat. Technol. 375 (2019) 215–220. https://doi.org/10.1016/j.surfcoat.2019.07.033.

[30] K. Huang, G. Wang, H. Qing, Y. Chen, H. Guo, Effect of Cu content on electrical resistivity, mechanical properties and corrosion resistance of AlCuxNiTiZr0.75 high entropy alloy films, Vacuum. 195 (2022) 110695. https://doi.org/10.1016/j.vacuum.2021.110695.

[31] H. Wang, J. Liu, Z. Xing, G.-Z. Ma, X. Cui, G. Jin, B. Xu, Microstructure and corrosion behaviour of AlCoFeNiTiZr high-entropy alloy films, Surf. Eng. 36 (2020) 78–85. https://doi.org/10.1080/02670844.2019.1625127.

[32] A. Leyland, A. Matthews, On the significance of the H/E ratio in wear control: a nanocomposite coating approach to optimised tribological behaviour, Wear. 246 (2000) 1–11. https://doi.org/10.1016/S0043-1648(00)00488-9.

[33] S.K. Bachani, C.-J. Wang, B.-S. Lou, L.-C. Chang, J.-W. Lee, Fabrication of TiZrNbTaFeN high-entropy alloys coatings by HiPIMS: Effect of nitrogen flow rate on the microstructural development, mechanical and tribological performance, electrical properties and corrosion characteristics, J. Alloys Compd. 873 (2021) 159605. https://doi.org/10.1016/j.jallcom.2021.159605.

[34] P.C. Pistorius, G.T. Burstein, Aspects of the effects of electrolyte composition on the occurrence of metastable pitting on stainless steel, Corros. Sci. 36 (1994) 525–538. https://doi.org/10.1016/0010-938X(94)90041-8.

[35] Y. Zhang, J.P. Liu, S.Y. Chen, X. Xie, P.K. Liaw, K.A. Dahmen, J.W. Qiao, Y.L. Wang, Serration and noise behaviors in materials, Prog. Mater. Sci. 90 (2017) 358–460. https://doi.org/10.1016/j.pmatsci.2017.06.004.

[36] M. Stern, A.L. Geary, Electrochemical Polarization: I . A Theoretical Analysis of the Shape of Polarization Curves, J. Electrochem. Soc. 104 (1957) 56. https://doi.org/10.1149/1.2428496.

[37] J.W. Schultze, M.M. Lohrengel, Stability, reactivity and breakdown of passive films. Problems of recent and future research, Electrochimica Acta. 45 (2000) 2499–2513. https://doi.org/10.1016/S0013-4686(00)00347-9.

[38] F. Moulder, W.F. Stickle, P.E. Sobol, K.D. Bomben, J. Chastain (Ed.), Handbook of X-ray photoelectron spectroscopy, Perkin-Elmer Corp, Eden Prairie, MN, 1992.

[39] K. Chong, Y. Gao, Z. Zhang, Y. Zou, X. Liang, Thermal stability and corrosion behavior of a novel Zr22.5Ti22.5Hf22.5Ni22.5Ta10 high-entropy amorphous alloy, Corros. Sci. 213 (2023) 110979. https://doi.org/10.1016/j.corsci.2023.110979.

[40] NIST X-ray Photoelectron Spectroscopy Database, NIST Standard Reference Database Number 20, National Institute of Standards and Technology, Gaithersburg MD, 20899 (2000), (n.d.). https://doi.org/10.18434/T4T88K.

[41] U. Veerabagu, P. Arumugam, Synthesis of Hf/SBA-15 Lewis acid catalyst for converting glycerol to value-added chemicals, J. Porous Mater. 24 (2017). https://doi.org/10.1007/s10934-016-0337-2.

[42] J. Jayaraj, C. Thinaharan, S. Ningshen, C. Mallika, U. Kamachi Mudali, Corrosion behavior and surface film characterization of TaNbHfZrTi high entropy alloy in aggressive nitric acid medium, Intermetallics. 89 (2017) 123–132. https://doi.org/10.1016/j.intermet.2017.06.002.

[43] Y.L. Hu, L.H. Bai, Y.G. Tong, D.Y. Deng, X.B. Liang, J. Zhang, Y.J. Li, Y.X. Chen, First-principle calculation investigation of NbMoTaW based refractory high entropy alloys, J. Alloys Compd. 827 (2020) 153963. https://doi.org/10.1016/j.jallcom.2020.153963.

[44] J. Wang, Y. Chen, Y. Zhang, Y. Zhang, J. Li, J. Liu, Y. Liu, W. Li, Microstructure evolution and acid corrosion behavior of CoCrFeNiCu1−xMox high-entropy alloy coatings fabricated by coaxial direct laser deposition, Corros. Sci. 198 (2022) 110108. https://doi.org/10.1016/j.corsci.2022.110108.

[45] E. Mak, B. Yin, W.A. Curtin, A ductility criterion for bcc high entropy alloys, J. Mech. Phys. Solids. 152 (2021) 104389. https://doi.org/10.1016/j.jmps.2021.104389.

[46] M.M. Garlapati, M. Vaidya, A. Karati, S. Mishra, R. Bhattacharya, B.S. Murty, Influence of Al content on thermal stability of nanocrystalline AlxCoCrFeNi high entropy alloys at low and intermediate temperatures, Adv. Powder Technol. 31 (2020) 1985–1993. https://doi.org/10.1016/j.apt.2020.02.032.

[47] S. Guo, C. Ng, J. Lu, C.T. Liu, Effect of valence electron concentration on stability of fcc or bcc phase in high entropy alloys, J. Appl. Phys. 109 (2011) 103505. https://doi.org/10.1063/1.3587228.

[48] S. Qiu, N. Miao, J. Zhou, Z. Guo, Z. Sun, Strengthening mechanism of aluminum on elastic properties of NbVTiZr high-entropy alloys, Intermetallics. 92 (2018) 7–14. https://doi.org/10.1016/j.intermet.2017.09.003.

[49] Y. Ke, F. Zahid, V. Timoshevskii, K. Xia, D. Gall, H. Guo, Resistivity of thin Cu films with surface roughness, Phys. Rev. B. 79 (2009) 155406. https://doi.org/10.1103/PhysRevB.79.155406.

[50] A.F. Mayadas, M. Shatzkes, Electrical-Resistivity Model for Polycrystalline Films: the Case of Arbitrary Reflection at External Surfaces, Phys. Rev. B. 1 (1970) 1382–1389. https://doi.org/10.1103/PhysRevB.1.1382.

[51] Y. Zhang, T. Zuo, Y. Cheng, P.K. Liaw, High-entropy Alloys with High Saturation Magnetization, Electrical Resistivity and Malleability, Sci Rep. 3 (2013) 1455. https://doi.org/10.1038/srep01455.

[52] W. Huo, X. Liu, S. Tan, F. Fang, Z. Xie, J. Shang, J. Jiang, Ultrahigh hardness and high electrical resistivity in nano-twinned, nanocrystalline high-entropy alloy films, Appl. Surf. Sci. 439 (2018) 222–225. https://doi.org/10.1016/j.apsusc.2018.01.050.

[53] H. Du, M. Zanáška, N. Brenning, U. Helmersson, Bipolar HiPIMS: The role of capacitive coupling in achieving ion bombardment during growth of dielectric thin films, Surf. Coat. Technol. 416 (2021) 127152. https://doi.org/10.1016/j.surfcoat.2021.127152.

[54] H. Du, M. Zanáška, U. Helmersson, D. Lundin, On selective ion acceleration in bipolar HiPIMS: A case study of (Al,Cr)2O3 film growth, Surf. Coat. Technol. 454 (2023) 129153. https://doi.org/10.1016/j.surfcoat.2022.129153.

[55] C.B. Nascimento, U. Donatus, C.T. Ríos, M.C.L. de Oliveira, R.A. Antunes, A review on Corrosion of High Entropy Alloys: Exploring the Interplay Between Corrosion Properties, Alloy Composition, Passive Film Stability and Materials Selection, Mater. Res. 25 (2022) e20210442. https://doi.org/10.1590/1980-5373-mr-2021-0442.

[56] L.F. Lin, C.Y. Chao, D.D. Macdonald, A Point Defect Model for Anodic Passive Films: II . Chemical Breakdown and Pit Initiation, J. Electrochem. Soc. 128 (1981) 1194. https://doi.org/10.1149/1.2127592.

[57] A. Raza, S. Abdulahad, B. Kang, H.J. Ryu, S.H. Hong, Corrosion resistance of weight reduced AlxCrFeMoV high entropy alloys, Appl. Surf. Sci. 485 (2019) 368–374. https://doi.org/10.1016/j.apsusc.2019.03.173.

[58] M. Li, Q. Chen, X. Cui, X. Peng, G. Huang, Evaluation of corrosion resistance of the single-phase light refractory high entropy alloy TiCrVNb0.5Al0.5 in chloride environment, J. Alloys Compd. 857 (2021) 158278. https://doi.org/10.1016/j.jallcom.2020.158278.

[59] Q. Zhao, Z. Pan, X. Wang, H. Luo, Y. Liu, X. Li, Corrosion and passive behavior of AlxCrFeNi3−x (x = 0.6, 0.8, 1.0) eutectic high entropy alloys in chloride environment, Corros. Sci. 208 (2022) 110666. https://doi.org/10.1016/j.corsci.2022.110666.

[60] H.-T. Hsueh, W.-J. Shen, M.-H. Tsai, J.-W. Yeh, Effect of nitrogen content and substrate bias on mechanical and corrosion properties of high-entropy films (AlCrSiTiZr)100−xNx, Surf. Coat. Technol. 206 (2012) 4106–4112. https://doi.org/10.1016/j.surfcoat.2012.03.096.

Table 1 Summary of the electrochemical parameters (averaged from 3 measurements). Corrosion potential (E_{corr}), corrosion current density (I_{corr}), Tafel anode slope (β_a), and Tafel cathode slope (β_c) are obtained by extrapolating the linear portion of polarization curves. The pitting potential (E_{pit}) and initial passivation current density (I_{pass}) are taken from potentiodynamic polarization curves of $(AlCr)_x(HfMoNbZr)_{1-x}$ films. The polarization resistance (R_p) is calculate using the Stern-Geary equation[36].

P_{AlCr} (W)	E_{corr} (mV)	I_{corr} (nA/cm^2)	β_a (mV)	β_c (mV)	R_p (kΩ·cm^2)	E_{pit} (mV)	I_{pass} (μA/cm^2)
0	331.82±15.88	11.0±1.9	91.74±8.66	40.23±0.8	1134.78	1350±72	3.49±0.2
50	358.82±30.76	5.46±0.47	80.57±5.68	44.23±0.46	2282.82	-	3.54±0.02
70	338.78±44.45	5.71±1.29	80.64±5.11	43.78±1.16	2280.05	-	3.64±0.01
90	364.74±40.57	4.85±0.43	79.52±6.13	44.97±1.77	2595.12	1359±99	3.66±0.02
110	396.62±59.75	7.54±1.33	72.87±6.42	42.82±0.47	1599.90	1312±54	3.81±0.03
130	435.14±41.76	6.05±1.77	69.67±6.34	44.75±5.34	2079.28	1259±65	3.64±0.05

List of figure captions

Fig. 1. Elemental composition of $(AlCr)_x(HfMoNbZr)_{1-x}$ films at the discharge power of AlCr target P_{AlCr} of 0 W, 50 W, 70 W, 90 W, 110 W, and 130 W.

Fig. 2. Cross-sectional SEM morphologies of $(AlCr)_x(HfMoNbZr)_{1-x}$ films deposited at P_{AlCr} of (a) 0 W, (b) 50 W, (c) 70 W, (d) 90 W, (e) 110 W, and (f) 130 W.

Fig. 3. (a) X-ray diffractograms and the X-ray diffractogram of $(AlCr)_{0.59}(HfMoNbZr)_{0.41}$ (calculated) crystal with the identical elemental composition with the film deposited at P_{AlCr} of 90 W. (b) out-of-plane lattice constant and calculated lattice constant, and (c) full width at half maximum (FWHM) at 110 peak of $(AlCr)_x(HfMoNbZr)_{1-x}$ films grown at various P_{AlCr}.

Fig. 4. (a) Hardness (H) and elastic modulus (E), and (b) H/E and H^3/E^{*2} of $(AlCr)_x(HfMoNbZr)_{1-x}$ films as a function of the AlCr target discharge power (P_{AlCr}).

Fig. 5. Electrical resistivity of $(AlCr)_x(HfMoNbZr)_{1-x}$ films as a function of P_{AlCr}.

Fig. 6. Potentiodynamic polarization curves of $(AlCr)_x(HfMoNbZr)_{1-x}$ films tested in 3.5 wt.% NaCl solution.

Fig. 7. High-resolution Hf 4f, Mo 3d, Nb 3d, Zr 3d, O 1s, Al 2p and Cr 2p spectra recorded from the HfMoNbZr film (P_{AlCr} = 0 W, (a) ~ (e)), and the AlCrHfMoNbZr film (P_{AlCr} = 90 W, (f) ~ (l)) with different etching depths. XPS spectra were taken for both films in the before and after corrosion states. Vertical lines indicate the reference binding energy values for metals (blue dashed lines), oxides (wine dashed lines), OH^- (black dashed lines) and Hf 4d (grey dashed lines).

Fig. 8. (a) The total density of states (TDOS) and (b) the partial density of states (PDOS) for Hf, Mo, Nb, Zr, Al, and Cr. TDOS and PDOS are obtained by the $(AlCr)_{0.59}(HfMoNbZr)_{0.41}$ alloy in accordance with the composition of $(AlCr)_x(HfMoNbZr)_{1-x}$ film grown at the target discharge power (P_{AlCr}) of 90 W. The Fermi energy is set to 0 eV and marked by vertical dashed lines.

Fig. 9. The electron localization function (ELF) of $(AlCr)_{0.59}(HfMoNbZr)_{0.41}$ compound in (001) plane. ELF = 0 and ELF = 1 correspond to the delocalized state and the localized state, respectively. The ELF = 0.5 corresponds to a uniform electron gas.

Fig. 1

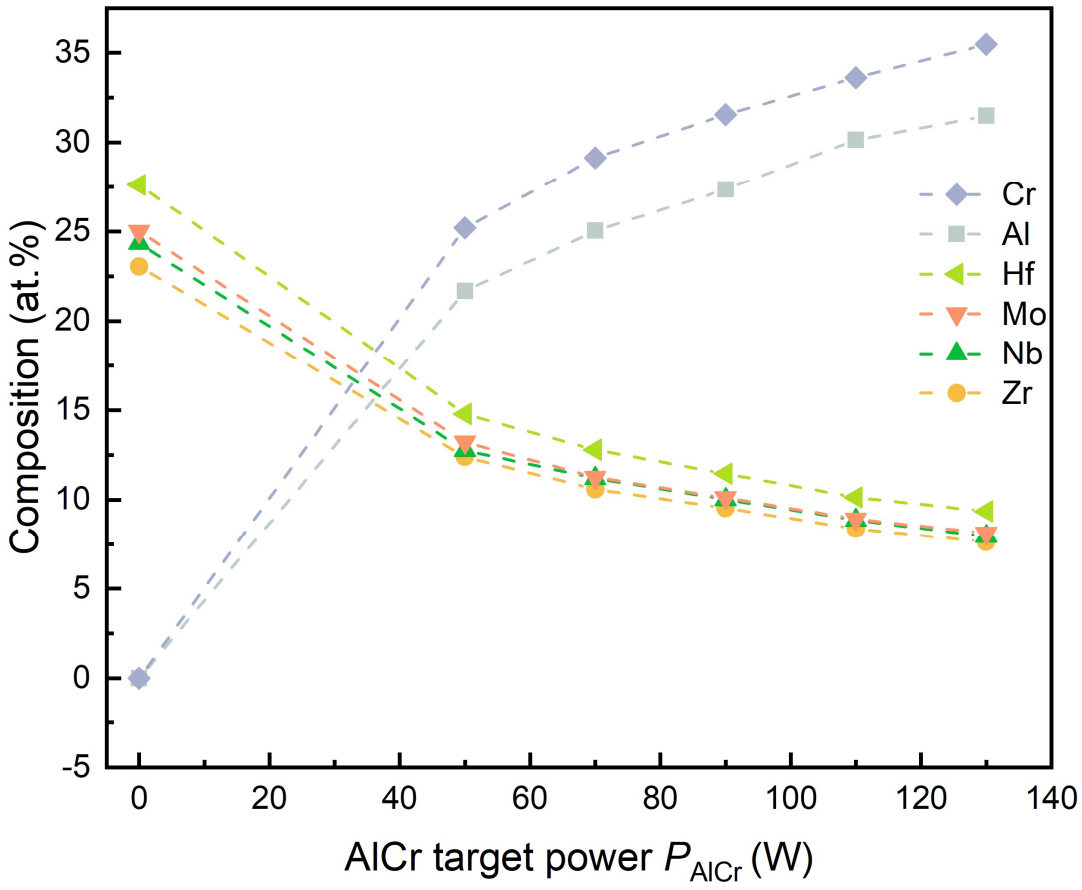

Fig. 1. Elemental composition of $(AlCr)_x(HfMoNbZr)_{1-x}$ films at the discharge power of AlCr target P_{AlCr} of 0 W, 50 W, 70 W, 90 W, 110 W, and 130 W.

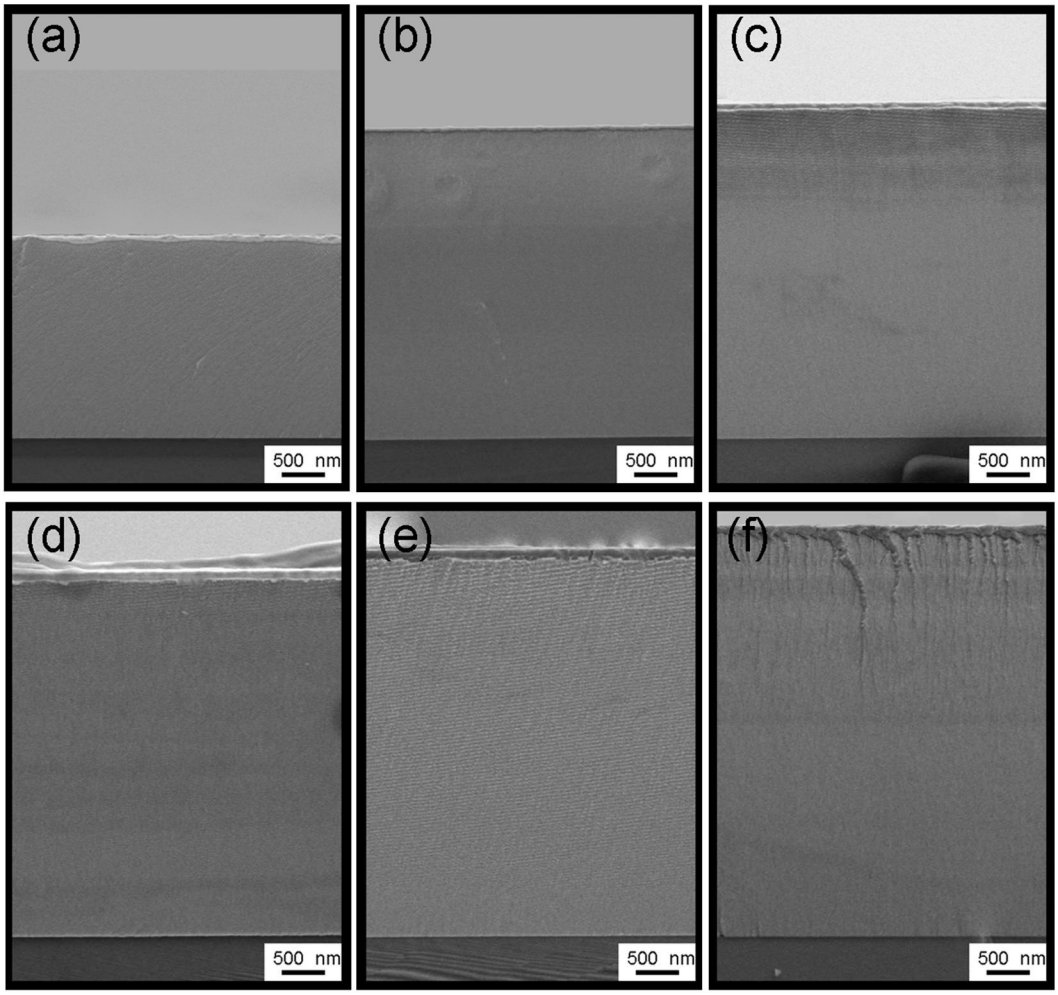

Fig. 2. Cross-sectional SEM morphologies of $(AlCr)_x(HfMoNbZr)_{1-x}$ films deposited at P_{AlCr} of (a) 0 W, (b) 50 W, (c) 70 W, (d) 90 W, (e) 110 W, and (f) 130 W.

Fig. 3

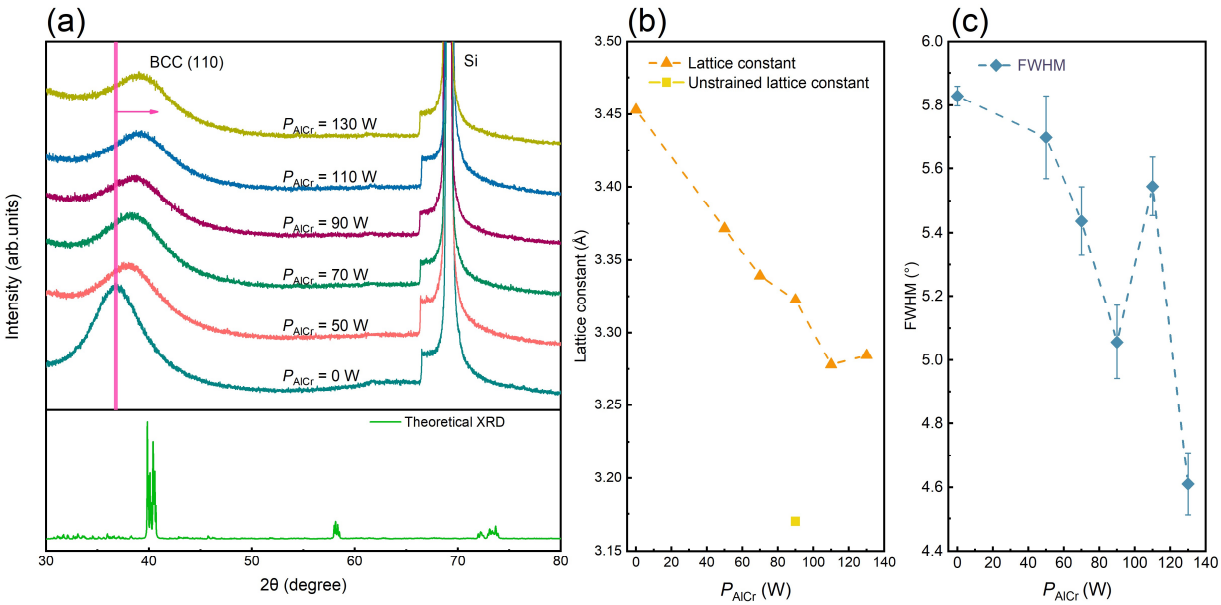

Fig. 3. (a) X-ray diffractograms and the X-ray diffractogram of $(AlCr)_{0.59}(HfMoNbZr)_{0.41}$ (calculated) crystal with the identical elemental composition with the film deposited at P_{AlCr} of 90 W. (b) out-of-plane lattice constant and calculated lattice constant, and (c) full width at half maximum (FWHM) at 110 peak of $(AlCr)_x(HfMoNbZr)_{1-x}$ films grown at various P_{AlCr}.

Fig. 4

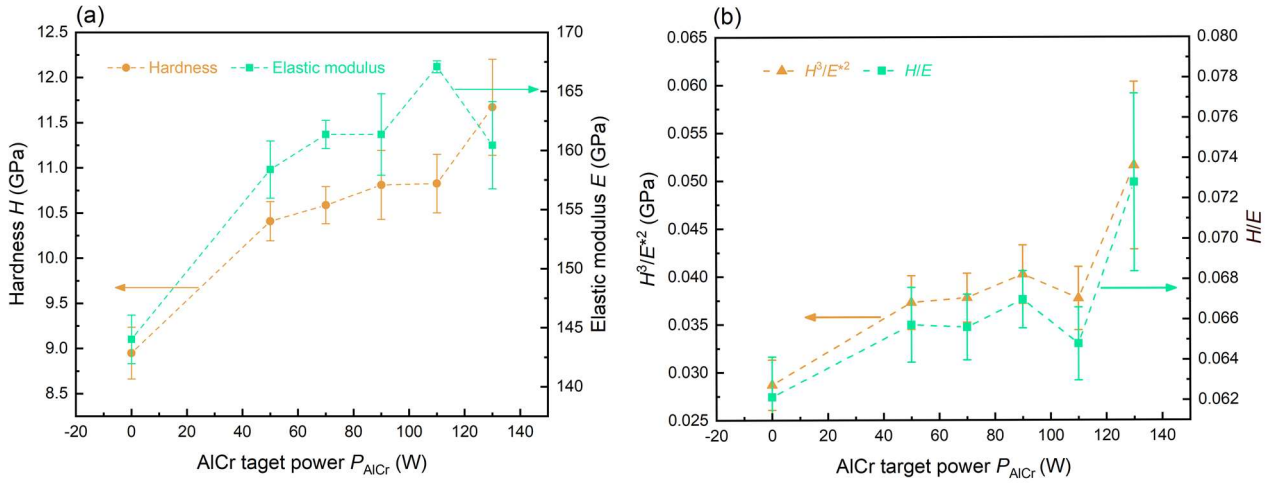

Fig. 4. (a) Hardness (H) and elastic modulus (E), and (b) H/E and H^3/E^{*2} of $(AlCr)_x(HfMoNbZr)_{1-x}$ films as a function of the AlCr target discharge power (P_{AlCr}).

Fig. 5

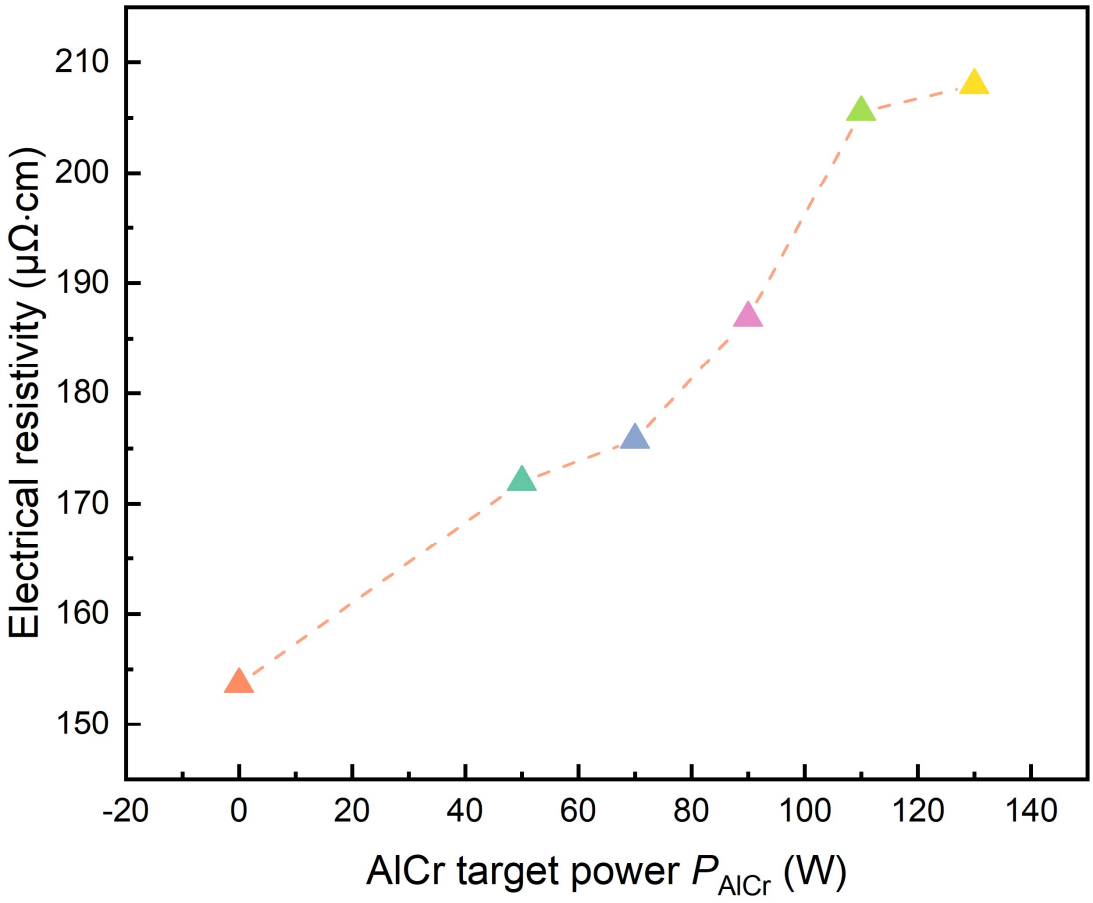

Fig. 5. Electrical resistivity of $(AlCr)_x(HfMoNbZr)_{1-x}$ films as a function of P_{AlCr}.

Fig. 6

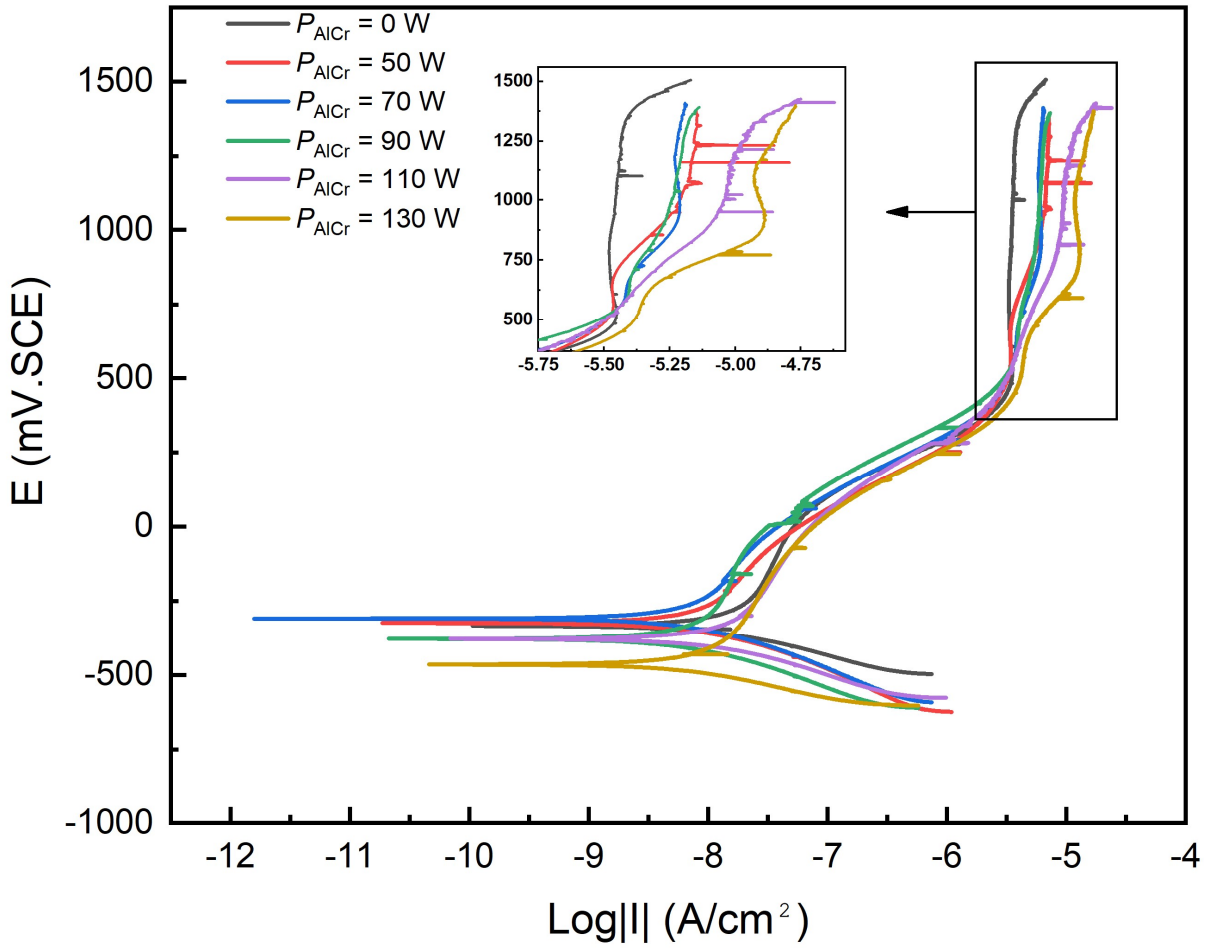

Fig. 6. Potentiodynamic polarization curves of $(AlCr)_x(HfMoNbZr)_{1-x}$ films tested in 3.5 wt.% NaCl solution.

Fig. 7

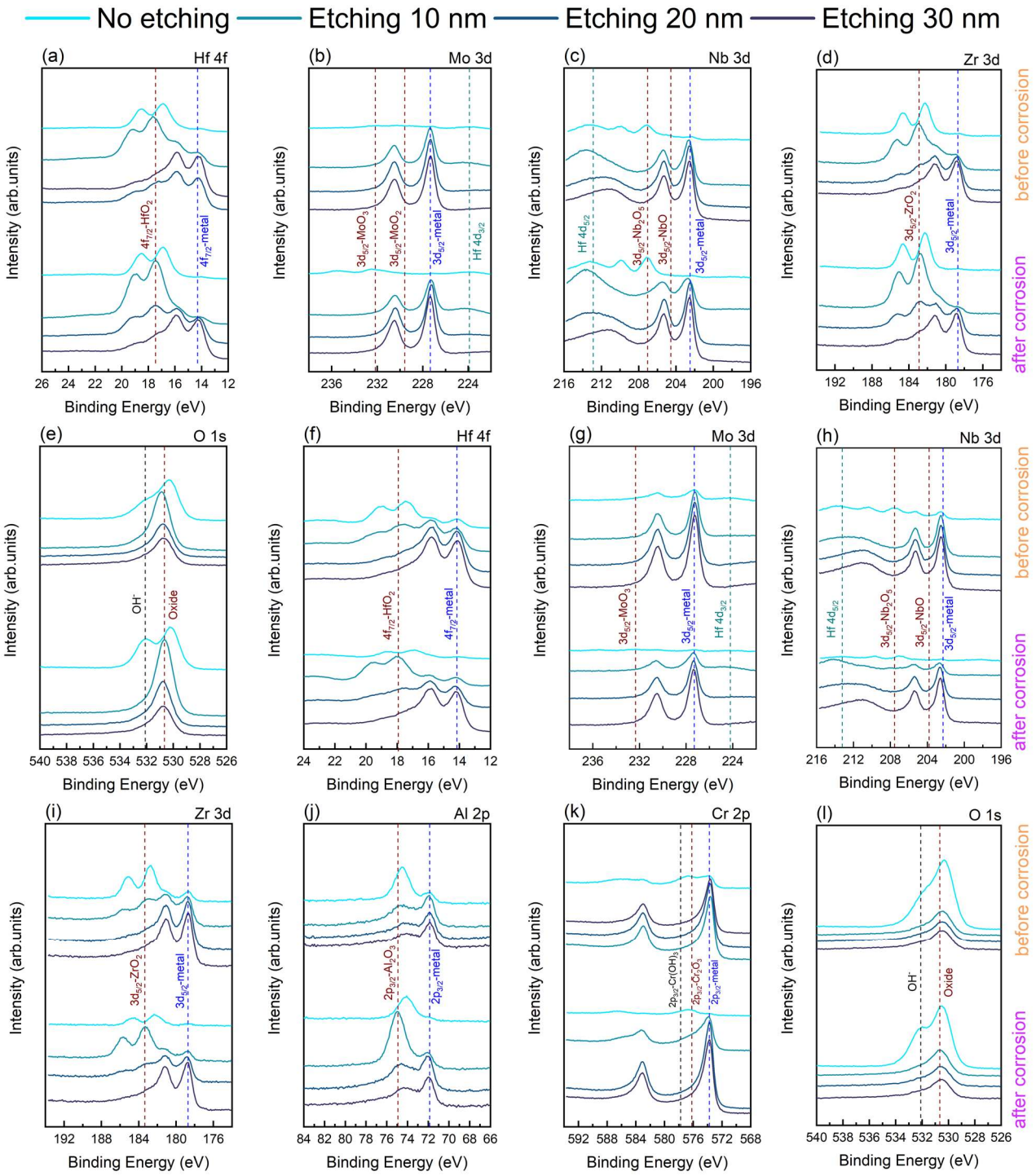

Fig. 7. High-resolution Hf 4f, Mo 3d, Nb 3d, Zr 3d, O 1s, Al 2p and Cr 2p spectra recorded from the HfMoNbZr film (P_{AlCr} = 0 W, (a) ~ (e)), and the AlCrHfMoNbZr film (P_{AlCr} = 90 W, (f) ~ (l)) with sputter-etching depths of 0, 10, 20, and 30 nm. XPS spectra were taken for both films in the before and after corrosion states. Vertical lines indicate the reference binding energy values for metals (blue dashed lines), oxides (wine dashed lines), OH^- (black dashed lines) and Hf 4d (grey dashed lines).

Fig. 8

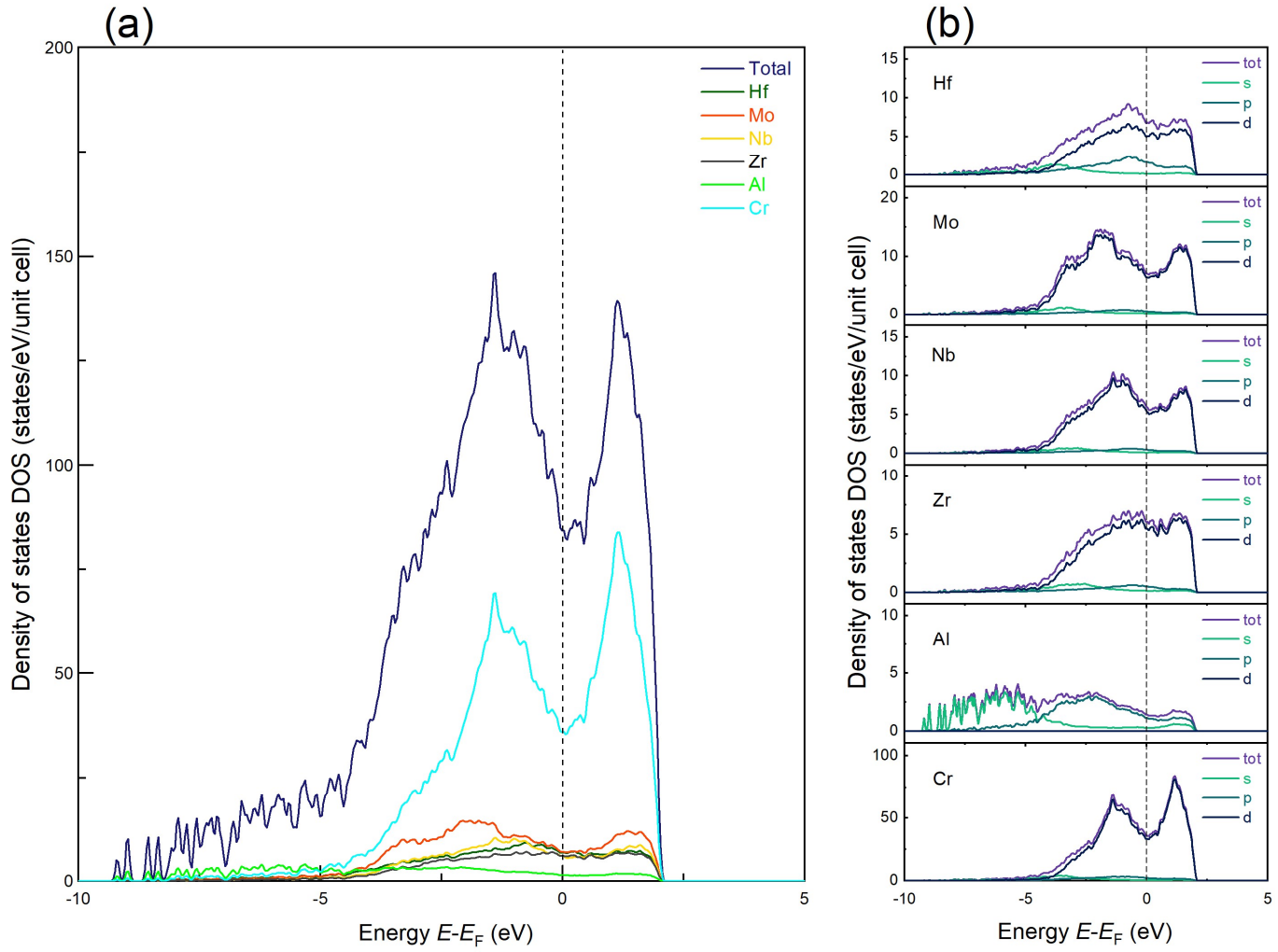

Fig. 8. (a) The total density of states (TDOS) and (b) the partial density of states (PDOS) for Hf, Mo, Nb, Zr, Al, and Cr. TDOS and PDOS are obtained by the $(AlCr)_{0.59}(HfMoNbZr)_{0.41}$ alloy in accordance with the composition of $(AlCr)_x(HfMoNbZr)_{1-x}$ film grown at the target discharge power (P_{AlCr}) of 90 W. The Fermi energy is set to 0 eV and marked by vertical dashed lines.

Fig. 9

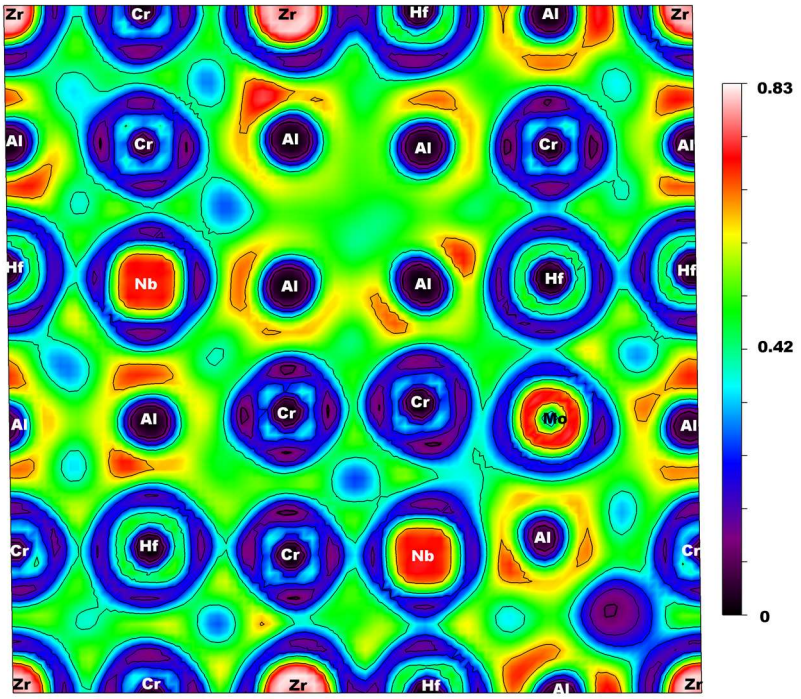

Fig. 9. The electron localization function (ELF) of $(AlCr)_{0.59}(HfMoNbZr)_{0.41}$ compound in (001) plane. ELF = 0 and ELF = 1 correspond to the delocalized state and the localized state, respectively. The ELF = 0.5 corresponds to a uniform electron gas.